Journal of Rock Mechanics and Geotechnical Engineering 14 (2022) 197–209

Contents lists available at ScienceDirect

Journal of Rock Mechanics and Geotechnical Engineering

journal homepage: www.jrmge.cn

Full Length Article

Influence of anisotropic stress path and stress history on stiffness of calcareous sands from Western Australia and the Philippines

Huan He [a], Siyue Li [b], Kostas Senetakis [c,*], Matthew Richard Coop [d], Songyu Liu [a]

[a] Institute of Geotechnical Engineering, Southeast University, Nanjing, 210096, China
[b] Department of Architecture and Civil Engineering, City University of Hong Kong, Kowloon, Hong Kong, China
[c] Department of Architecture and Civil Engineering, Yeung Kin Man Academic Building, Blue Zone 6/F, City University of Hong Kong, Kowloon, Hong Kong, China
[d] Department of Civil, Environmental and Geomatic Engineering, University College London, London, UK

ARTICLE INFO

Article history:
Received 11 January 2021
Received in revised form
24 February 2021
Accepted 31 March 2021
Available online 24 June 2021

Keywords:
Calcareous soils
Dynamic properties
Shear stiffness
Stress anisotropy
Stress history

ABSTRACT

Investigation of dynamic properties of carbonate/calcareous soils is important in earthquake and offshore engineering as these soils are commonly encountered in large-scale projects related with energy geomechanics and land reclamation. In this study, the stiffness and stiffness anisotropy of two types of calcareous sands (CS) from the Western Australia and the Philippines were examined using bender elements configured in different directions in stress path setups. Stiffness measurements were taken on specimens subjected to constant p' compression/extension and biaxial stress paths and additional tests were performed on three types of silica sands with different geological origins and particle shapes, which were used as benchmark materials in the study. Compared with the three brands of silica sands, the stiffness of the CS was found to be more significantly influenced by anisotropic loading; an important observation of the experimental results was that stress anisotropy had different weighted influences on the stiffness in different directions, thus influencing stiffness anisotropy. Comparisons were made between the specimens subjected to complex loading paths, and respected model parameters as suggested from published expressions in the literature. These comparisons further highlighted that calcareous soils have different responses in terms of stiffness, stiffness anisotropy and loading history, compared with that of silica-based sands.

1. Introduction

Calcareous sands (CS) are wide-spread in shallow sea environments, especially in tropical and sub-tropical regions, such as the South China Sea, the Red Sea, the west continental platform of Australia and Bass Strait (Alba and Audibert, 1999). They are often encountered in offshore projects, such as oil platforms, sub-sea infrastructures, and man-made islands (e.g. Wees and Chamberlin, 1971; McClelland, 1988; Brandes, 2011; Wang et al., 2011). Compared with typical silica sands, CS consists of particles with lower tensile strength and higher crushability and their properties are highly variant, due to the differences in biogenic types, geological origins, gradings, depths, and/or chemistry of the environment (Fookes, 1988; Coop, 1990; Miao and Airey, 2013). This gives uncertain characteristics to the mechanical behaviour of these soils and could, potentially, result in accidents or collapse of infrastructures founded on carbonate sediments (King and Lodge, 1988; Randolph and Gourvenec, 2011). Many research works have reported on the mechanical behaviour of CS with emphasis on large-deformation behaviour as well as the crushing behaviour of individual grains and assemblies of grains (Coop, 1990; Airey, 1993; Coop and Atkinson, 1993; Coop et al., 2004; Wang et al., 2011, 2017, 2018, 2020; Miao and Airey, 2013; Shahnazari and Rezvani, 2013; Wei et al., 2018; Yu, 2018; Lv et al., 2019). Despite these efforts and the importance of calcareous soils in large-scale and critical projects related with energy and land reclamation, there are relatively limited number of works investigating the stiffness characteristics of these complex soils, especially under very small strains and by applying complex loading paths, which represent, more effectively, the in situ stress-state of sediments and geological materials subjected to cyclic loads from vibrations or inclined loads from foundations.

* Corresponding author.
E-mail address: ksenetak@cityu.edu.hk (K. Senetakis).
Peer review under responsibility of Institute of Rock and Soil Mechanics, Chinese Academy of Sciences.

https://doi.org/10.1016/j.jrmge.2021.03.015

The stiffness of soils is critical to evaluate the seismic design of geo-structures and predict seismic ground response (Ishihara, 1996; Kramer, 1996) as it comprises a key property for soil characterization both under static and dynamic loadings (Clayton, 2011). Many studies on calcareous soils have focused on their small-strain stiffness under isotropic compression stress states (He et al., 2019; Morsy et al., 2019; Liu et al., 2020) or medium-to-large deformation behaviour (e.g. Coop, 1990; Airey, 1993; Coop and Atkinson, 1993; Coop et al., 2004; Miao and Airey, 2013; He et al., 2017a). In engineering practice, soils are often subjected to anisotropic stress states, such as fresh sediments in shallow seas, subsoil beneath foundations and soil close to slopes or dams. Nonetheless, only a few studies have examined the small-strain stiffness of calcareous soils under anisotropic stress conditions. Wang and Ng (2011), Senetakis and He (2017) and Jafarian and Javdanian (2020) stressed that constant mean effective stress (p') anisotropic loading affected notably the small-strain stiffness of crushable soils; the aforementioned studies examined completely decomposed granite and CS which, even though they are different materials in terms of origin and composition, they both have highly crushable grains. Therefore, a rather comprehensive understanding of the deformation characteristics (in terms of stiffness) of CS under anisotropic stress state is needed for enhancement of our predictive tools in engineering design as well as to provide further insights into the fundamental behaviour of these complex geo-materials.

To study the effect of stress anisotropy on the small-strain stiffness of calcareous soils, there are mainly two brands of anisotropic stress paths adopted by the majority of researchers, i.e. the constant p' stress path and the biaxial stress path (where "biaxial stress path" is often termed as "axisymmetric loading path"). Senetakis and He (2017) and Jafarian and Javdanian (2020) reported that under constant p' compression stress paths (where p' is kept constant and the deviatoric stress (q) gradually increased), the small-strain shear modulus (G_{max}) of CS increases. Fioravante et al. (2013) and Nanda et al. (2018) examined the small-strain stiffness of CS along biaxial stress paths, where one of the stress components is changed while keeping the others constant, to examine the sole effect of each stress component on stiffness. Previous studies stressed that the notable effect of stress anisotropy on the stiffness of CS cannot be ignored. However, the relationship and difference between the effects of different stress paths on carbonate sand stiffness, as well as the stiffness anisotropy induced by stress anisotropy, which can be critical for modelling, have been overlooked. Studies by Jovicic and Coop (1997) and He et al. (2019) showed that the over-consolidation ratio has a significant influence on the magnitude of stiffness of CS subjected to isotropic stress paths, which was reported to be a much less influential factor for quartz sands. However, there is a significant gap in the literature in understanding and quantifying the influence of anisotropic stress history on the small-strain stiffness of CS, which might be an important factor in modelling the small-strain behaviour of these complex soils.

Facing the insufficient understanding of the small-strain stiffness of calcareous soils subjected to anisotropic stress states, a systematic study on the small-strain stiffness of CS from two distinct origins under different stress paths was carried out in the present work. Bender element tests were performed on both loading and unloading phases of (i) constant p' and (ii) biaxial (or axisymmetric) stress paths. Three types of silica sands, which were used as benchmark materials, with different particle shapes and geological origins, were also studied. The empirical model parameters derived from the biaxial stress path tests were used to predict the shear stiffness of soils under isotropic and constant p' stress path, and the results are further discussed and analysed in the subsequent sections.

2. Materials and methods

2.1. Calcareous and silica sands studied

Two types of uncemented CS, from Western Australia (WA) and the Philippines (PH), were examined. Both types of CS originated from shallow sea environments but with different properties in terms of particle size, particle shape and composition. The grading curves and representative scanning electron microscope (SEM) images of both soils are given in Fig. 1. Observations of the SEM images suggest that both soils have a biogenic, rather than chemical, origin. The Philippines CS (PH-CS), which has a slightly higher specific gravity than the Western Australia CS (WA-CS), predominantly consists of dead coral reefs, while the WA-CS is composed of both dead coral reefs and shells. The basic properties of both CS are listed in Table 1. The particles of the PH-CS were coarser, with a higher mean grain size (D_{50}) value compared to the WA-CS (D_{50} equals to 0.23 mm and 0.50 mm for the WA-CS and the PH-CS, respectively), but the coefficients of uniformity for both soils were close (1.7 and 1.85 for the WA-CS and the PH-CS, respectively). Based on the unified soil classification system (USCS) (ASTM D2487-11, 2011), both types of geo-materials are classified as poorly graded sands (SP). The sphericity (S) and roundness (R) values of the two CSs were quantified through visual comparison from SEM images with respect to the empirical chart proposed by Krumbein and Sloss (1963), which was later modified by Cho et al. (2006) by introducing the shape descriptor of regularity (ρ_r) (summarised in Table 1). Regularity equals to the arithmetic mean of roundness and sphericity so that it captures quantitatively the "averaged" influence of different particle shape descriptors simultaneously. With lower average values of sphericity and roundness, the PH-CS was found to have grains of more irregular shape compared to the WA-CS. It was indicated that both types of CSs are composed, predominantly, of calcium compounds (normalised weight percentage of calcium exceeding 40%) based on energy dispersive spectroscopy (EDS) analysis (Table 1). Through a series of monotonic shearing tests, the critical state friction angle ($\phi_{critical}$) of the PH-CS was found to be 39.4°, which is higher compared with that of the WA-CS ($\phi_{critical} = 36.4°$). These differences are attributed predominantly to the higher angularity of the grains from the PH-CS.

Three types of silica sands from different geological environments were also tested in the current study for comparison,

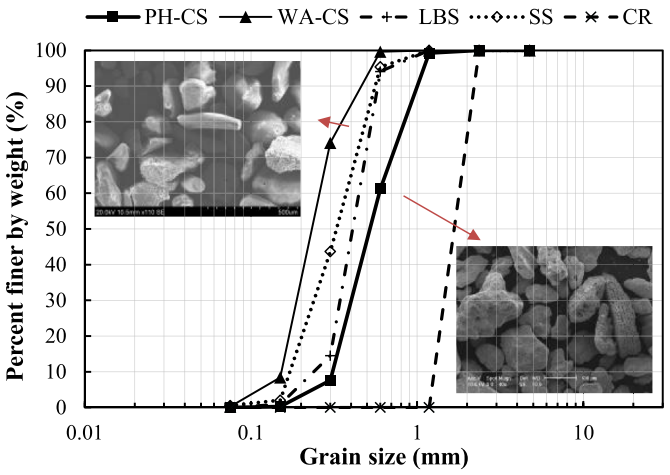

Fig. 1. Grading curves of the sands tested and SEM images for the WA-CS and the PH-CS. The CSs are illustrated in solid lines and the silica sands are presented in dashed lines.

Table 1
Basic characteristics of the WA-CS, the PH-CS and the reference silica sands (LBS, SS and CR).

Property	Value				
	WA-CS	PH-CS	LBS	SS	CR
Specific gravity, G_s	2.68	2.72	2.65	2.65	2.65
Mean grain size, D_{50} (mm)	0.23	0.5	0.41	0.33	1.67
Coefficient of uniformity, C_u	1.7	1.85	1.87	2.19	1.41
Coefficient of curvature, C_c	0.9	0.88	1.11	0.89	0.93
$\phi_{critical}$ (°)	36.4	39.4	–	–	–
Mean value of sphericity, S	0.6	0.53	0.77	0.76	0.51
Mean value of roundness, R	0.53	0.3	0.68	0.61	0.24
Mean value of regularity, ρ_r	0.57	0.42	0.7	0.69	0.38
Normalised silicon weight percentage (%)	1.8	0.42	–	–	–
Normalised calcium weight percentage (%)	41.2	44.6	–	–	–

including two silica sands with rounded grains: Leighton Buzzard sand (LBS), Sydney sand (SS) and a sand-sized uniform fraction of crushed rock (CR) (grain sizes: 1.18–2.36 mm) with angular particles. The grading curves of the silica sands are also presented in Fig. 1. SS is a natural material found in New South Wales, Australia, LBS is a material derived from clastic-sedimentary rock from the UK, and the CR was derived from a basaltic-type fine-grained igneous rock. The three types of silica-based sands represent three broad types of materials of comparatively strong grains but with various particle shapes and compositions. Basic properties of the silica sands, including specific gravity, mean grain size, coefficient of uniformity, coefficient of curvature, and particle shape parameters, are listed in Table 1.

2.2. Experimental method and specimen preparation

A stress-path triaxial apparatus with maximum capacity of 1 MPa, previously described by He et al. (2017b), was used in the study. The apparatus was supplied by GDS Inc. UK. A schematic plot of the apparatus is given in Fig. 2. The base pedestal and top cap

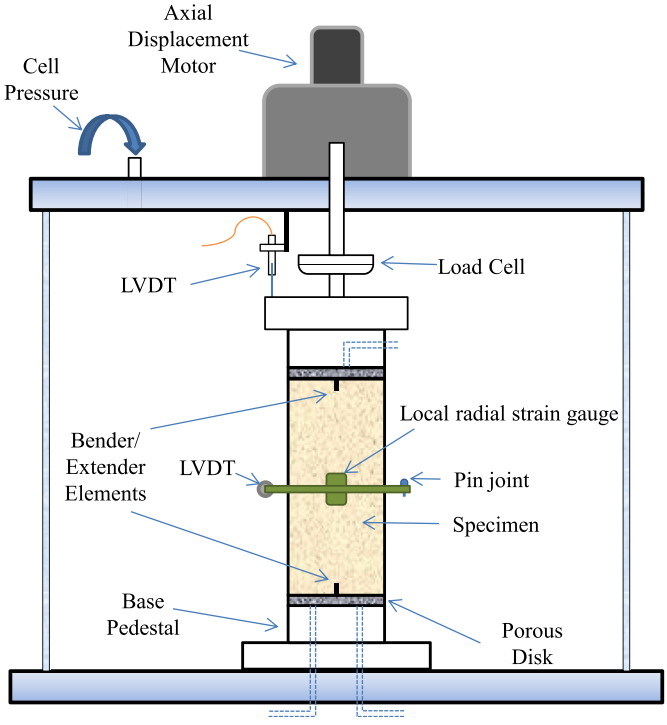

Fig. 2. Schematic illustration of the dynamic triaxial system with the local strain gauge (specimen diameter: 50 mm; specimen height: 100 mm).

were equipped with bender elements that are used to measure the shear wave velocities ($V_{s,vh}$) propagating in the vertical (along the axis of the specimen) direction. The apparatus is also equipped with a back volume controller. The radial strain gauges paired with the vertically mounted linear variable differential transformers (LVDTs) were used as an alternative technique to record the volume changes during the tests, especially for dry specimens.

A custom-modified Bishop and Wesley (BW) triaxial apparatus (which was introduced by Li and Senetakis (2017) and Todisco et al. (2018)). with embedded bender elements was also used in the study (a schematic plot of the apparatus is given in Fig. 3). This apparatus was supplied by Imperial College London, UK. A custom-built local radial strain gauge (after Ackerley et al., 2016) was used in the BW triaxial system to monitor the radial strains of the specimens. Both vertical and lateral bender element systems were implemented into the BW triaxial apparatus. The lateral bender element system consisted of two pairs of piezo-elements configured in T-shape, i.e. one pair is placed vertically and the other pair is placed horizontally, which can be used to measure $V_{s,hv}$ (the velocity of the shear waves which travel horizontally and induce vertical particle motion) and $V_{s,hh}$ (the velocity of shear waves which travel horizontally and induce horizontal particle motion), respectively, and the configuration was initially designed by Pennington et al. (2001). A schematic plot of the arrangements of the vertical and lateral bender elements is given in Fig. 4. Representative illustration of the transmitted shear wave is given in Appendix A, where the first time of arrival method for signal interpretation is also shown. The validation of the signal interpretation method was presented by He and Senetakis (2016) and He et al. (2019).

The specimens were prepared in a dry state in layers using the dry compaction method. The initial void ratio of the specimen was controlled by varying the applied compaction energy. Most of the specimens were tested in a dry state, while some of the WA-CS specimens were tested in a fully saturated state. Notably, only vertical bender element tests were performed for the WA-CS specimens, while both vertical and lateral bender element tests were performed for the PH-CS specimens.

2.3. Testing program and stress paths

The details of the specimens and the applied stress paths are given in Table 2 for the WA-CS specimens and in Table 3 for the PH-CS and the silica sand specimens. The anisotropic stress paths adopted in the study are illustrated in Fig. 5, where the markers represent the stress states where the bender element tests were performed. Measurements of wave velocities and stiffness were performed during both loading and unloading of the anisotropic stress paths for most of the specimens, so that to explore the influence of loading history apart from the influence of stress path.

The constant p' of anisotropic stress path was adopted for the majority of the tests. During the constant p' anisotropic stress paths, the deviatoric stress (q) increased (in compression tests) or decreased (in extension tests) while keeping p' constant after the specimen was isotropically compressed initially to a certain magnitude of p' (as illustrated in Fig. 5a), where $q = \sigma'_a - \sigma'_r$, $p' = (\sigma'_a + 2\sigma'_r)/3$, σ'_a is the effective axial stress, and σ'_r is the effective radial stress. In order to maintain p' constant and change q, σ'_a and σ'_r are changed in opposite directions, i.e. σ'_a increases while σ'_r decreases in constant p' compression, denoted as "Comp." (or alternatively σ'_a decreases while σ'_r increases in constant p' extension, denoted as "Ext."). The maximum stress ratio ($\eta = q/p'$) reached during the compression tests was 1.2, and the minimum stress ratio reached under the extension tests was $\eta = -0.5$.

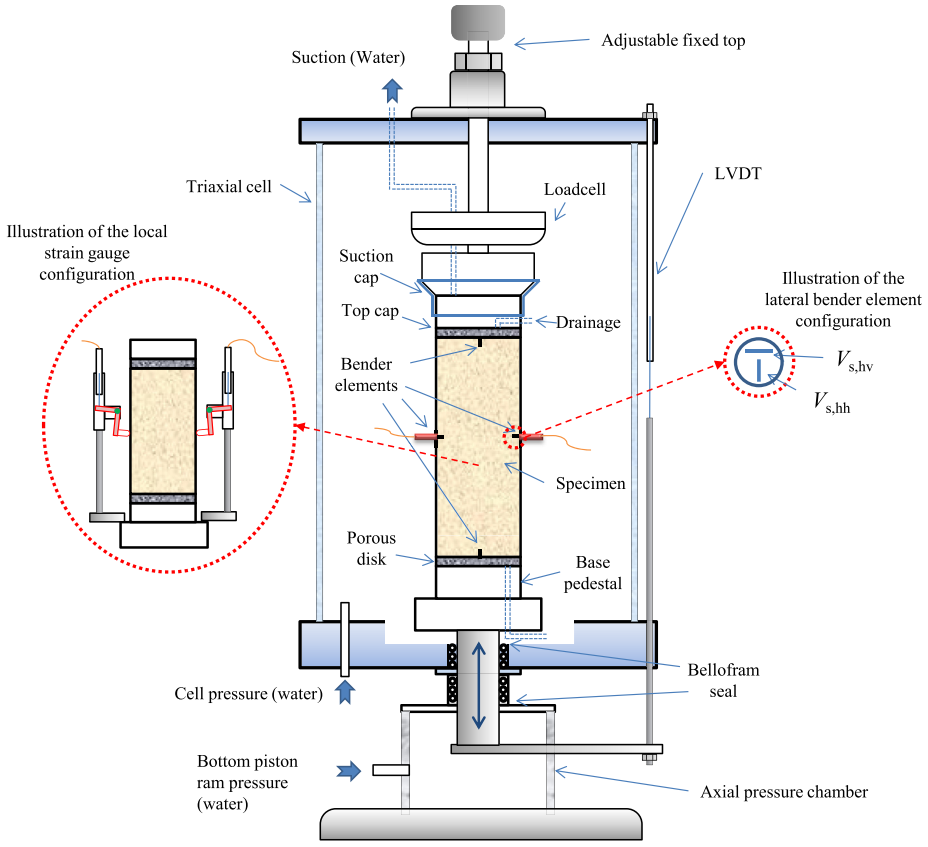

Fig. 3. Schematic illustration of the BW triaxial system with both vertical and lateral bender elements and the local radial strain gauges (specimen diameter: 50 mm; specimen height: 100 mm).

Apart from the constant p' stress paths, the small-strain shear moduli of the PH-CS specimens, including G_{vh}, G_{hv} and G_{hh} (shear moduli derived from $V_{s,vh}$, $V_{s,hv}$ and $V_{s,hh}$, respectively), were also measured along constant σ'_a and constant σ'_r stress paths, during which the magnitude of one stress component is kept constant while altering the other stepwise (as illustrated in Fig. 5b). The constant σ'_r-constant σ'_a type of stress path (shown in Fig. 5c) was adopted to avoid extension stress states, where $\sigma'_r > \sigma'_a$, along the stress path.

3. Results and discussion

3.1. Results

3.1.1. Constant p' anisotropic compression/extension stress paths test results – loading phase

The stiffness-stress ratio relationship of a soil subjected to a constant p' anisotropic stress path test can be expressed by (Payan et al., 2016a):

$$[G_{vh\ ani}/f(e_{ani})]/[G_{vh\ iso}/f(e_{iso})] = (\eta+1)^{\alpha_{G,vh}} \quad (1)$$

$$f(e) = e^{-1.29} \quad (2)$$

where $G_{vh\ ani}$ and $G_{vh\ iso}$ are the small-strain shear moduli under constant p' anisotropic stress state and isotropic stress state, respectively; e_{ani} and e_{iso} are the corresponding void ratios; and $\alpha_{G,vh}$ is a model constant. The stiffness is normalised with respect to a void ratio function (Eq. (2)) to eliminate possible influences from the changes in void ratio among different specimens. The term η on the right side of Eq. (1) represents the stress ratio (equal to q/p'). From a set of anisotropic compression loading tests on different silica sands, Payan et al. (2016a) reported that the exponent $\alpha_{G,vh}$ is a function of the coefficient of uniformity (C_u) and particle shape (expressed with the shape descriptor of regularity, ρ_r), and they proposed the following equation:

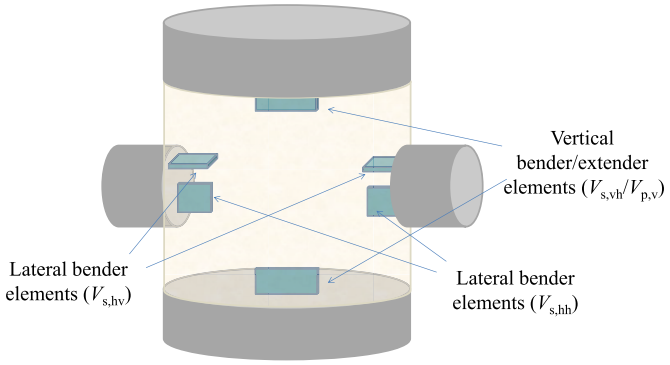

Fig. 4. Schematic illustration of vertical and horizontal bender/extender elements and the type of wave velocity measured (not in scale).

$$\alpha_{G,vh} = 0.017C_u^{0.40}\rho_r^{-1.82} \quad (3)$$

The normalised shear modulus ($[G_{vhani}/f\ (e_{ani})]/[G_{vhiso}/f\ (e_{iso})]$) against $\eta+1$ plots of representative specimens from two types of CS are given in Fig. 6a. Based on the C_u and ρ_r of the two types of CS (WA-CS: $C_u = 1.7$, $\rho_r = 0.565$; PH-CS: $C_u = 1.85$, $\rho_r = 0.415$), the

Table 2
Specimen details of WA-CS.

No.	Code	Initial void ratio, e_o	Saturation status	Stress path	p' (kPa)
1	WA-01	1.265	Dry	Constant p' compression	100
2	WA-02	1.323	Dry	Constant p' compression	200
3	WA-03	1.193	Dry	Constant p' compression	400
4	WA-04	1.202	Saturated	Constant p' compression	100
5	WA-05	1.192	Saturated	Constant p' compression	200
6	WA-06	1.191	Saturated	Constant p' compression	400
7	WA-07	1.357	Dry	Constant p' compression	400
8	WA-08	1.165	Dry	Constant p' compression	100
9	WA-09	1.167	Dry	Constant p' compression	200
10	WA-10	1.371	Dry	Constant p' extension	100
11	WA-11	1.38	Dry	Constant p' extension	200
12	WA-12	1.323	Dry	Constant p' extension	400
13	WA-13	1.313	Saturated	Constant p' extension	200
14	WA-14	1.305	Saturated	Constant p' extension	400
15	WA-15	1.305	Dry	Constant p' extension	400

anisotropic compression loading $\alpha_{G,vh}$ values for WA-CS and PH-CS are predicted to be 0.06 and 0.11, respectively, from Eq. (3). Both CS exhibited higher $\alpha_{G,vh}$ exponent values in comparison with what the empirical equation predicted. Since the empirical equation proposed by Payan et al. (2016a) was developed based on quartz soils, it is understood that the shear stiffness of the CS is more greatly influenced by the stress anisotropy compared with quartz sands of the same grading and particle shape. It is observed that the stiffness component G_{vh} of the PH-CS specimens had slightly higher sensitivity to the anisotropic compression compared with the WA-CS specimens, which is manifested by the higher average $\alpha_{G,vh}$ exponent value of the PH-CS specimens (average $\alpha_{G,vh}$ of PH-CS equals to 0.144) compared with that of the WA-CS specimens (average $\alpha_{G,vh}$ of WA-CS equals to 0.11), as listed in Tables 4 and 5. Note that at a given p', the axial strains induced by the constant p' anisotropic loading for the two brands of CS were found to be close. Thus, the higher $\alpha_{G,vh}$ values observed from the PH-CS specimens were not likely induced by strains, but were rather influenced by the lower grain regularity of the PH-CS in comparison with the WA-CS (Payan et al., 2016a). No clear effect of the saturation state (i.e. dry or fully saturated specimens) on the small-strain stiffness under anisotropic stress states was identified, given the close exponent values of the dry and saturated WA-CS specimens.

For constant p' anisotropic extension tests, the stiffness of representative WA-CS specimens, which are illustrated by hollow markers in Fig. 6b, dropped by around 0–5%, while the stiffness for the PH-CS specimens slightly increased (presented in solid markers in Fig. 6b), as η decreased from 0 to −0.5. In general, the stiffness component G_{vh} for both CS was only slightly influenced by the decrease of the stress ratio ($\eta = q/p'$) under extension stress states. From Tables 4 and 5, it can be noticed that the constant p' extension $\alpha_{G,vh}$ values for both sands were close to zero, but the average value for the WA-CS was positive, while that for the PH-CS was negative.

3.1.2. Constant p' anisotropic compression/extension stress paths test results – unloading phase

Representative plots of normalised stiffness against η+1 for both loading and unloading phases of the anisotropic stress states are given in Fig. 7a and b for WA-CS and PH-CS. These data suggest that the stiffness of both soils under the unloading stage deviated from the loading stage, i.e. the anisotropic loading history affects notably the magnitude of the stiffness. Adopting a similar approach as the data analysis during the loading phase, the test results of the unloading phase of both sands were fitted by the power law expression given in Eq. (1), and the derived values of the unloading exponent ($\alpha_{UG,vh}$) are listed in Tables 4 and 5 The average unloading exponent values for anisotropic compression are 0.012 and −0.029 for WA-CS and PH-CS, respectively, representing a limited change in stiffness during the unloading process of the anisotropic compression. On the other hand, the unloading of the anisotropic extension affected more pronouncedly the stiffness G_{vh} of both sands, with the average $\alpha_{UG,vh}$ values for the anisotropic extension stress paths to be equal to 0.115 and 0.120 for WA-CS and PH-CS, respectively. It is therefore understood that the stress history may have a different influence on the stiffness in different directions, contributing in this way to further anisotropic behaviour of the calcareous sands. This may have important implications in geomechanics modelling and geophysical characterization of sediments, as this behaviour has not been reported in the literature for quartz-based sands.

Table 3
Specimen details of PH-CS, LBS, SS and CR.

No.	Specimen code	Initial void ratio, e_o	Saturation status	Stress path	p' (kPa)	$\sigma'_{a,min}$ (kPa)	$\sigma'_{a,max}$ (kPa)	$\sigma'_{r,min}$ (kPa)	$\sigma'_{r,max}$ (kPa)
1	PH-01	0.97	Dry	Constant p' compression	100	100	180	60	100
2	PH-02	1.001	Dry	Constant p' compression	200	300	540	180	300
3	PH-03	0.995	Dry	Constant p' compression	300	200	333	133	200
4	PH-04	0.92	Dry	Constant p' compression	500	500	900	300	500
5	LBS	0.602	Dry	Constant p' compression	100	100	180	60	100
6	PH-05	0.995	Dry	Constant p' extension	200	133	200	200	233
7	PH-06	0.942	Dry	Constant p' extension	200	133	200	200	233
8	PH-07	0.999	Dry	Constant p' extension	300	200	300	300	350
9	PH-08	1	Dry	Constant p' extension	500	333	500	500	583
10	PH-09	1.018	Dry	Constant σ'_r	–	100	380	100	100
11	PH-10	1.087	Dry	Constant σ'_r	–	200	760	200	200
12	PH-11	0.993	Dry	Constant σ'_a	–	100	100	100	330
13	PH-12	0.994	Dry	Constant σ'_a	–	200	200	200	660
14	PH-15	1.087	Dry	Constant σ'_r - constant σ'_a	–	200	600	200	600
15	SS	0.653	Dry	Constant σ'_r - constant σ'_a	–	200	600	200	600
16	CR	0.605	Dry	Constant σ'_r - constant σ'_a	–	200	600	200	600

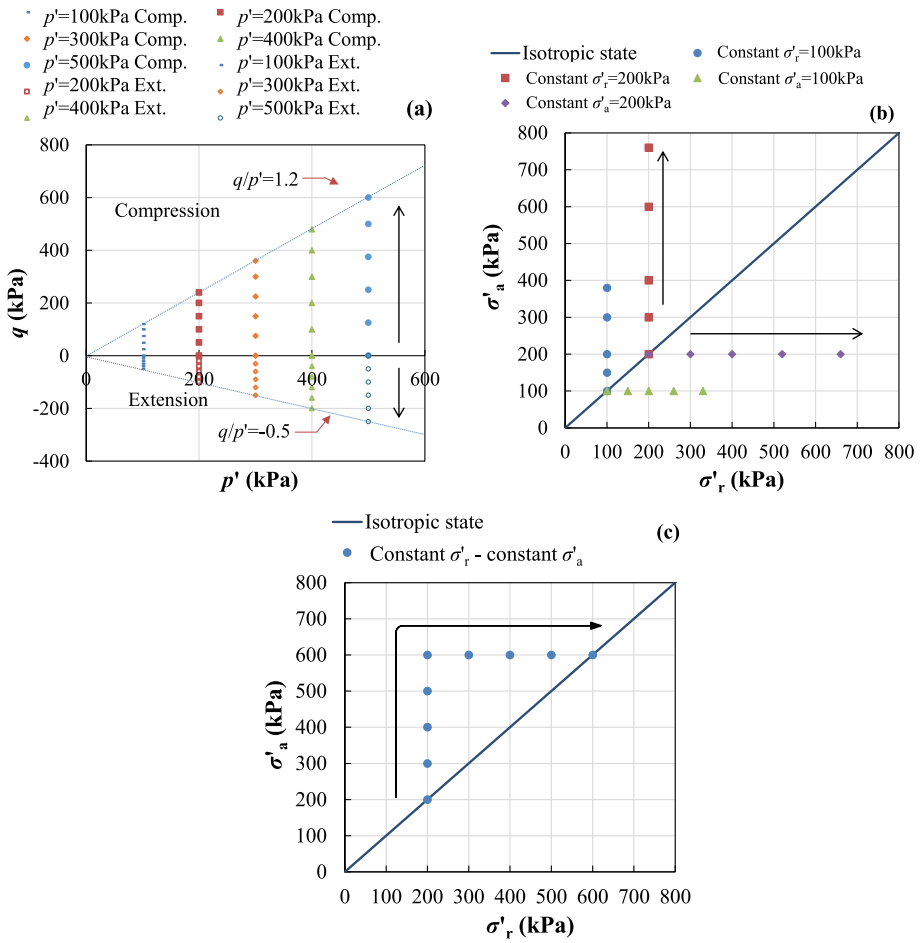

Fig. 5. Illustration of the anisotropic stress paths followed (the data points represent the stress states where bender element tests were conducted): (a) Constant p' compression and extension stress paths on the q-p' plane, (b) Constant σ'_a and constant σ'_r stress paths on the σ'_a-σ'_r plane, and (c) Constant σ'_r-constant σ'_a stress path on the σ'_a-σ'_r plane.

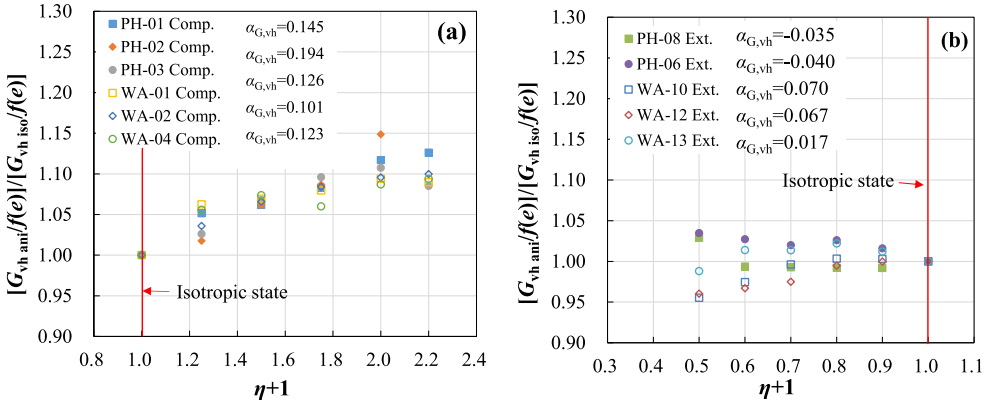

Fig. 6. Representative plots of normalised G_{vh} against η+1 for both types of CS subjected to (a) anisotropic compression stress paths and (b) anisotropic extension stress paths.

The effect of anisotropic stress history on the stiffness of specimens from LBS and the PH-CS (PH-01) is illustrated in Fig. 8, in terms of normalised G_{vh} against η+1 plots. G_{vh} of the LBS specimen was less affected by the stress anisotropy compared with that of the PH-CS specimen, with a maximum shear modulus increase of the order of 4%–5% at $\eta = 1$, and the anisotropic compression loading exponent $\alpha_{G,vh}$ of the LBS specimen was found to be equal to 0.073. Different from the tests on the CS, no significant effect of the anisotropic loading history was observed for the LBS specimen. The stiffness component G_{vh} along the unloading path was found to be slightly lower than that of the corresponding loading phase of the anisotropic stress path (Fig. 8). The lower value of the exponent $\alpha_{G,vh}$ and the small effect of the anisotropic loading history on the LBS specimen are attributed, predominantly, to the less significant fabric changes induced by the anisotropic stress in the LBS specimen compared with the more pronounced influences observed for the CS.

The stiffness component, G_{hv}, of the PH-CS specimens was also measured along constant p' anisotropic stress paths, and the

Table 4
Constant p' anisotropic stress path test details for WA-CS.

No.	Specimen code	Compression or extension	p' (kPa)	Exponent $\alpha_{G,vh}$	Unloading exponent $\alpha_{UG,vh}$
1	WA-01	Compression	100	0.101	0.031
2	WA-02	Compression	200	0.123	0.034
3	WA-03	Compression	400	0.124	0.031
4	WA-04	Compression	100	0.098	0.008
5	WA-05	Compression	200	0.113	0.001
6	WA-06	Compression	400	0.094	0.007
7	WA-07	Compression	400	0.105	−0.028
8	WA-08	Compression	100	0.12	–
9	WA-09	Compression	200	0.11	–
			Average	0.11	0.012
			Standard deviation	0.011	0.012
10	WA-10	Extension	100	0.07	0.12
11	WA-11	Extension	200	0.084	0.126
12	WA-12	Extension	400	0.067	0.103
13	WA-13	Extension	200	0.017	0.126
14	WA-14	Extension	400	0.088	0.117
15	WA-15	Extension	400	0	0.095
			Average	0.054	0.115
			Standard deviation	0.048	0.101

stiffness-stress ratio relationship of G_{hv} was similar to that of G_{vh}. By plotting the exponent values of G_{vh} and G_{hv} of individual tests in Fig. 9, it was revealed that the $\alpha_{G,hv}$ and $\alpha_{G,vh}$ exponent values for both the anisotropic compression and extension stress paths are close in magnitude. However, the compression exponent $\alpha_{G,hv}$ was always slightly lower compared with the exponent $\alpha_{G,vh}$ (the average $\alpha_{G,hv}$ and $\alpha_{G,vh}$ values equal to 0.107 and 0.144, respectively, from Table 5). These observations agree with the data presented by Gu et al. (2017), who found that the G_{hv} component was less affected by the axial compressive stress anisotropy compared to the G_{vh} component based on numerical analyses using the discrete element method (DEM).

3.1.3. Stiffness anisotropy under constant p′ anisotropic stress paths tests

Systematic fabric anisotropy was not observed in the reconstituted PH-CS specimens under isotropic stress conditions from the recent study by He et al. (2019). In the present study, the stiffness anisotropy induced by anisotropic stress was examined for one of the PH-CS specimens and the LBS specimen, by comparing the G_{hv} and G_{hh} measured from the two sets of lateral bender elements in the BW stress path triaxial system. The data in Fig. 10a suggest that at isotropic state, where $\eta+1$ equals 1, no significant stiffness anisotropy could be observed (G_{hh}/G_{hv} is close to unity), but the stress anisotropy induced noticeable stiffness anisotropy. As $\eta+1$ reached a value of 2, the ratio G_{hh}/G_{hv} decreased to 0.83. This observation can be explained by the stiffness–stress relationship in different directions. G_{hh} is affected predominantly by the horizontal (radial) stress component, while G_{hv} is affected by both the vertical and horizontal stress components since the particle contacts in the horizontal direction tend to be weakened by the application of the anisotropic compression (e.g. Oda et al., 1985; Rothenburg and Bathurst, 1992; Cheng, 2018). The ratio between G_{hh} and G_{hv} during the unloading stages of the anisotropic compression is also plotted in Fig. 10a. The data suggest that after the removal of the stress anisotropy, i.e. the stress ratio η is reduced from unity to zero, the stiffness anisotropy was not completely removed for the PH-CS specimen, with the ratio G_{hh}/G_{hv} reaching a value of 0.92. From DEM analyses, Gu et al. (2013) reported that the stiffness anisotropy might remain in the specimen after the anisotropic loading is removed because of the permanent fabric changes caused by the deviatoric stress.

As for the test on the LBS, it was observed that the ratio G_{hh}/G_{hv} reached 0.81 at $\eta = 1$, representing evident stiffness anisotropy, which is similar to what was found for the PH-CS specimen. However, the stiffness anisotropy was removed entirely for the LBS specimen after the anisotropic stress was unloaded (Fig. 10b). This difference between the silica sand and the CS, in terms of the effect of anisotropic loading history on the stiffness anisotropy, has been overlooked in the literature, but the data from the present study suggest that these sands with different origins have a completely different behaviour against anisotropic loading history.

Fig. 11 shows a plot of the axial strain against $\eta+1$ for both PH-2 and LBS specimens. These data suggest that although the maximum induced strain was relatively small in magnitude (0.38% for the calcareous sand at $\eta = 1$ and 0.15% for the silica sand), plastic deformations were dominant in both types of sands (PH-2 and LBS). This "residual" stiffness anisotropy of the CS may be attributed to the higher angularity and lower tensile strength of its particles, which resulted in irrecoverable fabric changes and strain induced anisotropy during the application of the anisotropic stress path. For the LBS, which has more rounded grains with higher tensile strength, the stiffness anisotropy is considered to be predominantly the result of stress induced anisotropy, since the plastic strains remained in the specimens did not lead to notable stiffness anisotropy. This hypothesis can be further supported by previous studies on the influence of particle shape on the stiffness-pressure relationship of granular materials subjected to anisotropic stress state (Cho et al., 2006; Payan et al., 2016a).

3.1.4. Test results of constant σ'_a and constant σ'_r stress path

Under biaxial and true triaxial loading, it has been reported that the predominant stress components which influence shear modulus are the principal stress along the wave propagation direction, denoted as σ'_i, and the principal stress along the particle motion direction, denoted as σ'_j, while the out of plane stress has a negligible influence (Roesler, 1979; Knox et al., 1982; Stokoe et al., 1985; Bellotti et al., 1996; Santamarina and Cascante; 1996; Fioravante et al., 2013). Based on the studies by Roesler (1979), Yu and Richart (1984), Ni (1987) and Hardin and Blandford (1989), the following general empirical formula has been proposed:

$$G_{max} = A_{ij} f(e) (\sigma'_i)^{n_i} \left(\sigma'_j\right)^{n_j} p_n^{-n_i-n_j} \quad (4)$$

where A_{ij}, n_i, and n_j are the constants; while n_i and n_j describe the sensitivity of G_{max} to the stress along the wave propagation direction and the particle motion direction, respectively.

Five specimens from the PH-CS, one specimen from the silica SS and one specimen from the silica CR were tested following constant σ'_a or constant σ'_r stress paths so that to examine the effect of σ'_i and σ'_j, individually, on the different stiffness components. Representative results on the PH-CS are illustrated in Fig. 12a and b for constant σ'_r and constant σ'_a tests, respectively. For the PH-CS, the average n_i (= 0.353) was found to be higher than the average n_j value (= 0.278), which suggests that the stress in the wave propagation direction has a higher impact on stiffness in comparison with the influence of the stress in the particle motion direction. The data in the unloading phases in Fig. 12 show that the stiffness was increased by the anisotropic stress loading history and that the exponent values are smaller in magnitude during the unloading process (un_i and un_j) compared with the loading process (n_i and n_j). A summary of the data for the loading and unloading exponent values for all the constant σ'_a and constant σ'_r stress path tests is given in Table 6.

The (n_i, n_j) values for the SS and the CR specimens were found to be equal to (0.207, 0.188) and (0.348, 0.265), respectively, as illustrated in Fig. 13. The data in this figure suggest that the exponent values n_i of the

Table 5
Constant p' anisotropic stress path test details for PH-CS.

No.	Specimen code	Compression or extension	p' (kPa)	Exponent $\alpha_{G,vh}$	Unloading exponent $\alpha_{UG,vh}$	Exponent $\alpha_{G,hv}$	Unloading exponent $\alpha_{UG,hv}$
1	PH-01	Compression	100	0.145	0.025	0.093	−0.096
2	PH-02	Compression	200	0.194	−0.02	0.174	−0.061
3	PH-03	Compression	300	0.126	−0.077	0.098	−0.094
4	PH-04	Compression	500	0.11	−0.042	0.062	−0.074
			Average	0.144	−0.029	0.107	−0.081
			Standard deviation	0.036	0.043	0.048	0.017
5	PH-05	Extension	200	0.075	–	0.033	–
6	PH-06	Extension	200	−0.04	0.114	0.002	0.115
7	PH-07	Extension	300	−0.089	0.124	−0.112	0.124
8	PH-08	Extension	500	−0.035	0.121	−0.032	0.093
			Average	−0.022	0.12	−0.027	0.111
			Standard deviation	0.069	0.005	0.062	0.016

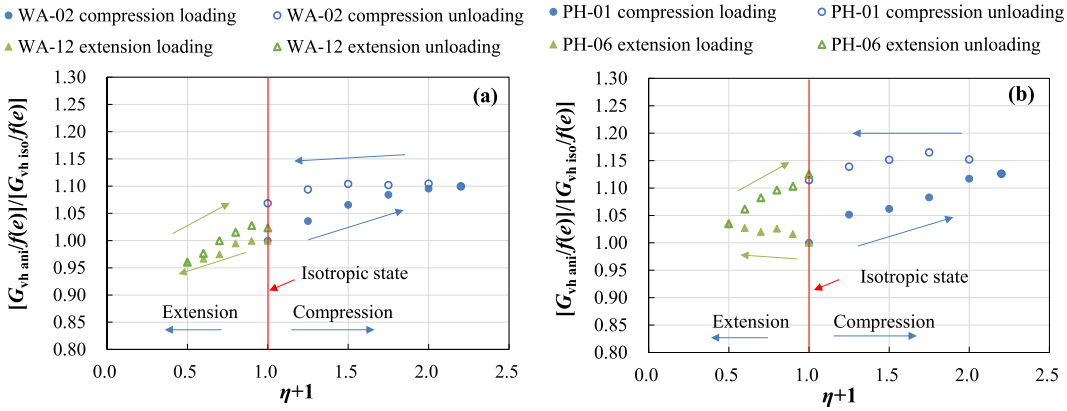

Fig. 7. Representative plots of normalised G_{vh} against $\eta+1$ for both types of CS during loading and unloading of constant p' anisotropic compression and extension: (a) WA-02 (anisotropic compression) and WA-12 (anisotropic extension), and (b) PH-01 (anisotropic compression) and PH-06 (anisotropic extension).

silica sands were also greater in magnitude compared with their corresponding n_j values (Table 6). Note that the horizontal axis of Fig. 13 represents σ'_a when depicting the results along the constant σ'_r stress path (lower curve in the figure), while it represents σ'_r when depicting the results along the constant σ'_a stress path (upper curve in the figure). Although for the two types of silica sands and the PH-CS calcareous sand, the n_i values are always higher than the n_j values, it was observed that compared with the angular sands, the difference between the n_i and n_j of the SS was much smaller (specifically, the average n_i-n_j values for the PH-CS, the CR and the SS were 0.075, 0.083 and 0.019, respectively). The positive n_i-n_j values imply that the stress in the wave propagation direction has a stronger influence on small-strain shear stiffness than the stress in the direction of particle motion. In the studies by Roesler (1979), Knox et al. (1982) and Viggiani and Atkinson (1995), the magnitude of n_i was reported to be greater than that of n_j. However, Yu and Richart (1984), Santamarina and Cascante (1996), Fioravante (2000) and Fioravante et al. (2013) observed the opposite trends. Yu and Richart (1984) indicated that the end restraint of their resonant column may also have an influence, while the difference between n_i and n_j values is found to be dependent on the mineralogy/composition and particle shape from the current study.

The loading and unloading exponent values n_i, un_i, n_j and un_j are compared in Fig. 14. As illustrated in Fig. 13a and b, during the unloading process, the sensitivity of the stiffness to the stress component is reduced compared with that in the loading process. Both un_i and un_j decreased more than 65% compared with the corresponding values in the loading process for the PH-CS, with the exponent un_i (average $un_i = 0.111$) to be greater than the exponent un_j (average $un_j = 0.075$). Examining a washed quartz mortar sand, Knox et al. (1982) did not observe any significant drop of the exponent values from their constant σ'_r and constant σ'_a loading-unloading tests.

3.2. Discussion

3.2.1. Comparison between the summation of n_i and n_j with the isotropic exponent n_G

At isotropic stress state, the stress components are equal in magnitude ($\sigma'_i = \sigma'_j = p'$), and the following expression can be derived from Eq. (4):

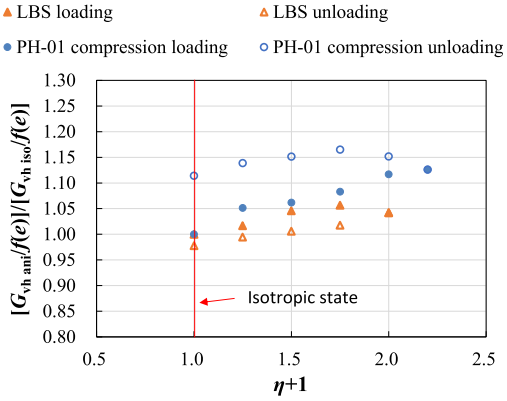

Fig. 8. Comparison of normalised G_{vh} of constant p' compression tests during loading and unloading stress paths of LBS and PH-CS.

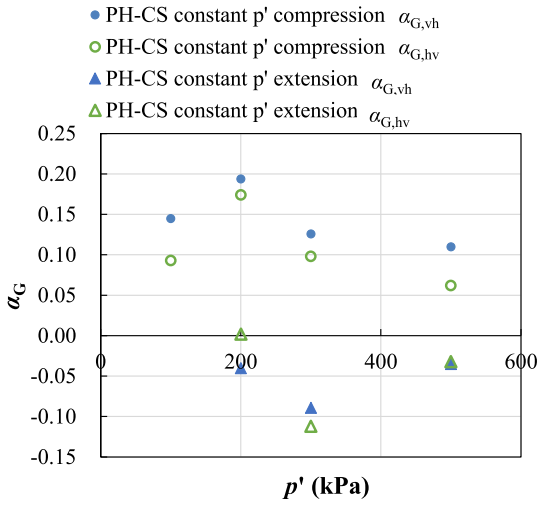

Fig. 9. $\alpha_{G,vh}$ and $\alpha_{G,hv}$ against p' for four tests of PH-CS.

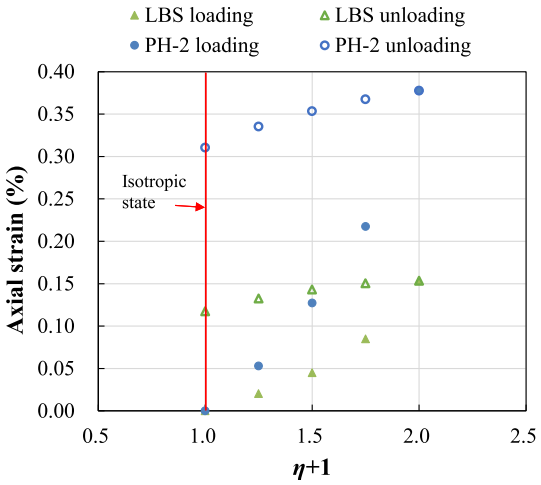

Fig. 11. Axial strain against $\eta+1$ during constant p' anisotropic compression tests for specimens LBS and PH-2.

$$G_{max} = A_{ij} f(e)(\sigma'_i)^{n_i}\left(\sigma'_j\right)^{n_j} p_n^{-n_i-n_j} = A_{ij} f(e)\left(\frac{p'}{p_n}\right)^{n_i+n_j} \quad (5)$$

The right side of the equation is widely adopted to describe the stiffness of soils under isotropic stress paths, and the term $(n_i + n_j)$ can be denoted as n_G. Thus, theoretically, the exponent n_G for isotropic compression should be equal to the summation of n_i and n_j.

Previous works (e.g. Roesler, 1979; Knox et al., 1982; Viggiani and Atkinson, 1995; Fioravante et al., 2013) found rather good agreements between the summation of n_i and n_j with the exponent n_G. In the current study, the summation of n_i and n_j ($n_i + n_j = 0.4$) for SS was found to be close to the n_G value reported by Payan et al. (2016b) (taking into account the given particle shape of the SS, would predict a value $n_G = 0.43$). However, the summation of the average n_i and n_j of the PH-CS and the CR in this study are 0.631 and 0.613, respectively, which are both much higher than the average exponent values (PH-CS: $n_G = 0.48$, CR: $n_G = 0.53$) that would be predicted from the proposed expressions by He et al. (2019) and Payan et al. (2016b) for the condition of isotropic stress path. Under an anisotropic stress state, the fabric of soils with angular particles is hypothesized to be altered more pronouncedly compared to soils with rounded particles, which may be, predominantly, because of a higher level of interlocking, lower coordination number and stress redistribution (Gu et al., 2013, 2017). This could explain the differences between the summation of n_i and n_j and the isotropic n_G for the PH-CS and the silica CR.

3.2.2. *Prediction of the stiffness of the sands subjected to constant p′ stress paths with the measured n_i and n_j values*

With the knowledge of the n_i and n_j values of a geo-material, the shear modulus at any given stress state should, theoretically, be predicted from Eq. (4). At an anisotropic stress state, the small-strain shear modulus ($G_{vh\ ani}$) could be expressed by the following expression based on Eq. (4):

$$G_{vh\ ani} = A_{ij} f(e_{ani})\left(\sigma'_{i,ani}\right)^{n_i}\left(\sigma'_{j,ani}\right)^{n_j} p'^{-n_i-n_j}_n \quad (6)$$

where $\sigma'_{i,ani}$ and $\sigma'_{j,ani}$ are the effective stresses in the direction of wave propagation and in the direction of particle motion at anisotropic stress state. Substituting the anisotropic and isotropic

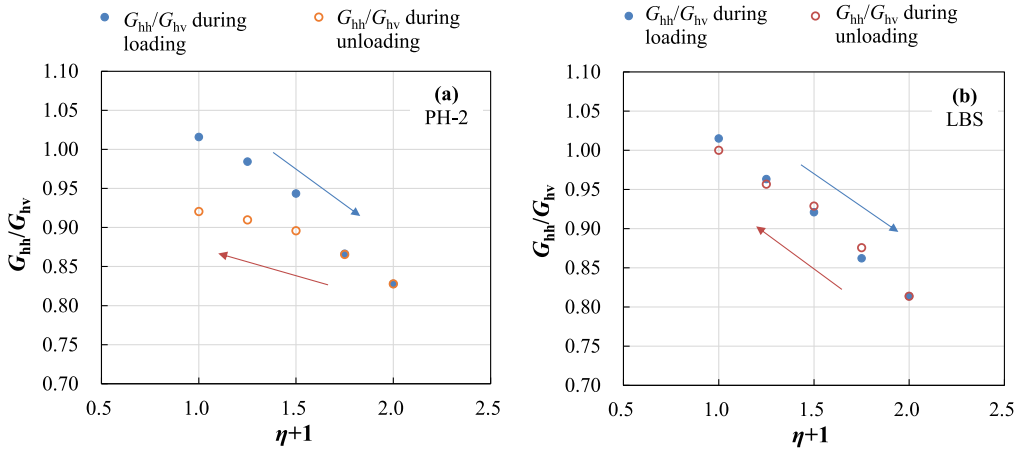

Fig. 10. G_{hh}/G_{hv} against $\eta+1$ during constant p' anisotropic compression tests for (a) a representative specimen of the PH-CS, and (b) an LBS specimen.

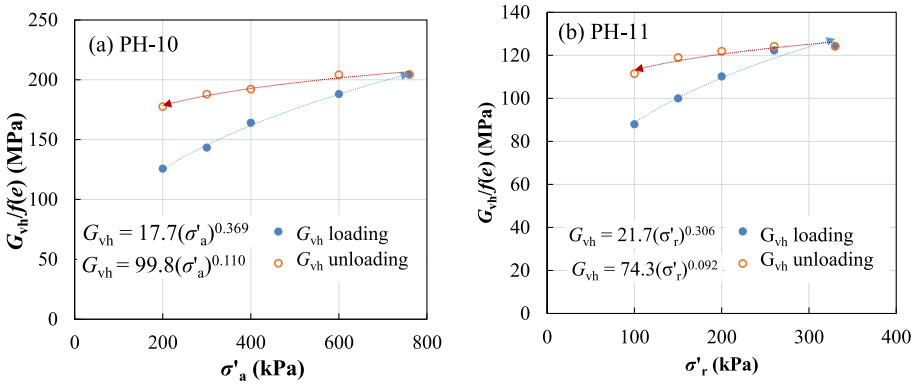

Fig. 12. Representative results of constant σ'_a and constant σ'_r tests: (a) Normalised shear modulus $G_{vh}/f(e)$ against effective axial stress σ'_a for specimen PH-10, and (b) Normalised shear modulus $G_{vh}/f(e)$ against effective radial stress σ'_r for specimen PH-11.

Table 6
Exponent values from PH-CS, SS and CR tests.

Specimen code	Constant stress (kPa)	Direction of shear modulus	n_i	n_j	un_i	un_j
PH-09	$\sigma'_r = 100$	G_{vh}	0.362	–	0.112	–
PH-10	$\sigma'_r = 200$	G_{vh}	0.369	–	0.11	–
PH-15	$\sigma'_r = 200$	G_{vh}	0.329	–	–	–
PH-11	$\sigma'_a = 100$	G_{vh}	–	0.306	–	0.092
PH-12	$\sigma'_a = 200$	G_{vh}	–	0.252	–	0.057
PH-15	$\sigma'_a = 600$	G_{vh}	–	0.276	–	–
		Average	0.353	0.278	0.111	0.075
		Standard deviation	0.021	0.027	0.001	0.025
SS	$\sigma'_r = 200$	G_{vh}	0.207	–	–	–
SS	$\sigma'_a = 600$	G_{vh}	–	0.188	–	–
CR	$\sigma'_r = 200$	G_{vh}	0.348	–	–	–
CR	$\sigma'_a = 600$	G_{vh}	–	0.265	–	–

stiffness (G_{vhani}, G_{vhiso}) of the left side of Eq. (1) with the calculation given in Eq. (6), the following expression can be derived:

$$[G_{vh\ ani}/f(e_{ani})]/[G_{vh\ iso}/f(e_{iso})] = (1.8)^{n_i}(0.6)^{n_j} = (\eta+1)^{\alpha_{G,vh}} \quad (7)$$

An attempt was made to predict the stiffness-stress ratio relationship of the PH-CS under constant p' stress paths based on the measured n_i and n_j values from Eq. (7), and the predicted values are compared with the constant p' stress path test results (based on the laboratory measurements). Taking constant p' anisotropic compression as an example, when the stress ratio ($\eta = q/p'$) equals 1.2, $\sigma'_{i,ani} = 1.8\ \sigma'_{i,iso}$ and $\sigma'_{j,ani} = 0.6\ \sigma'_{j,iso}$, under which cases, Eq. (7) can be re-written as

$$[G_{vh\ ani}/f(e_{ani})]/[G_{vh\ iso}/f(e_{iso})] = (1.8)^{n_i}(0.6)^{n_j} = (\eta+1)^{\alpha_{G,vh}} = 2.2^{\alpha_{G,vh}} \quad (8)$$

Taking the average n_i (=0.353) and n_j (=0.278) exponent values into the equation, the normalised stiffness ($[G_{vh\ ani}/f(e_{ani})]/[G_{vh\ iso}/f(e_{iso})]$) is predicted to be 1.068 at $\eta = 1.2$, i.e. the normalised stiffness with respect to void ratio would increase by 6.8% as the stress ratio increases from 0 to 1.2. From the set of constant p' stress path tests, the measured average $\alpha_{G,vh}$ is 0.144, which makes the right side of the equation equal 1.12, suggesting that the measured stiffness would increase by 12% as the stress ratio increases from 0 to 1.2. For SS, the stiffness component G_{vh} should increase by 2.6% as η increases from 0 to 1.2 based on the measured n_i (=0.201) and n_j (=0.188) values, and this predicted magnitude of stiffness increase matches well with the predicted values based on the proposed expression by Payan et al. (2016a).

The results from the constant σ'_a and constant σ'_r stress path tests suggest that the unloading exponent values (un_i and un_j) were notably different from the loading exponent values (n_i and n_j). Considering that σ'_r decreases during a constant p' compression stress path and σ'_a decreases during a constant p' extension stress path, the unloading exponent values (un_i or un_j), theoretically, should be adopted for the stiffness prediction where the stress component decreases along the stress paths. A flow chart is plotted in Fig. 15a to illustrate the predictions of change of the stiffness

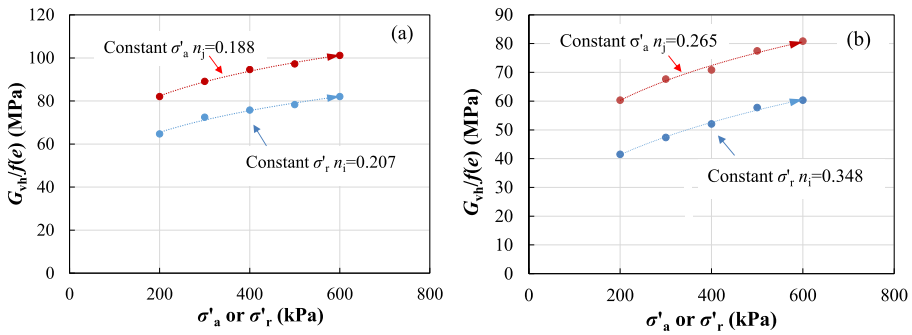

Fig. 13. Representative results of constant σ'_a and constant σ'_r tests: (a) Normalised shear modulus $G_{vh}/f(e)$ against σ'_a and σ'_r for Sydney sand specimen, and (b) Normalised shear modulus $G_{vh}/f(e)$ against σ'_a and σ'_r for crushed rock specimen.

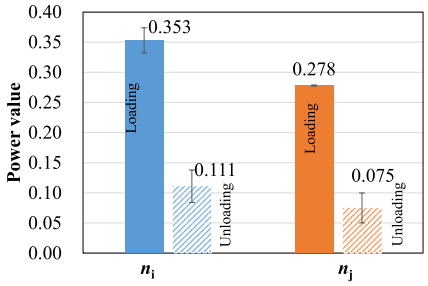

Fig. 14. Average loading and unloading n_i, n_j, un_i and un_j values of the PH-CS with the corresponding standard deviation illustrated.

components (G_{vh} and G_{hv}) under both constant p' anisotropic compression and extension with different combinations of n_i, n_j, un_i and un_j values. The predicted values of the percentage of stiffness change are compared with the "measured" values in Fig. 15b, where the "measured" change of shear stiffness under anisotropic stress states was calculated with the average α_G values derived based on constant p' stress path tests. It is noticed that the predictions of G_{vh} under constant p' extension stress state, as well as G_{hv} under both constant p' compression and extension stress states, based only on loading exponents (n_i, n_j) notably deviate from the measured values. However, adopting the "loading and unloading exponents" to predict the stiffness under constant p' anisotropic stress states yielded rather satisfactorily accurate results.

Under constant p' anisotropic stress states, the stiffness-stress ratio (η) relationship of sand depends, predominantly, on the relationship between n_i (or un_i) and n_j (or un_j) of the soil. For a given material, if the n_i is much larger than the un_j, the shear stiffness component G_{vh} will increase along the constant p' compression stress path (where q/p' increases). Otherwise (when n_i is smaller than un_j), the stiffness component G_{vh} will be not sensitive to constant p' anisotropic compression. A series of theoretical plots of normalised stiffness ($[G_{vh\ ani}/f\ (e_{ani})]/[G_{vh\ iso}/f\ (e_{iso})]$) against the stress ratio (η+1) is presented in Fig. 16, where the effect of the change of un_j on the stiffness-stress ratio relationship under constant p' compression stress path is illustrated. As un_j increased from 0.1 to 0.3 while keeping n_i constant at 0.2, the normalised stiffness decreased under constant p' anisotropic compression stress states, which suggests lower α_G values. Based on Eq. (3), Payan et al. (2016a) reported that α_G values were found to be higher for sands with more angular particles and/or with a higher coefficient of uniformity, and higher α_G values further imply that the n_i exponent

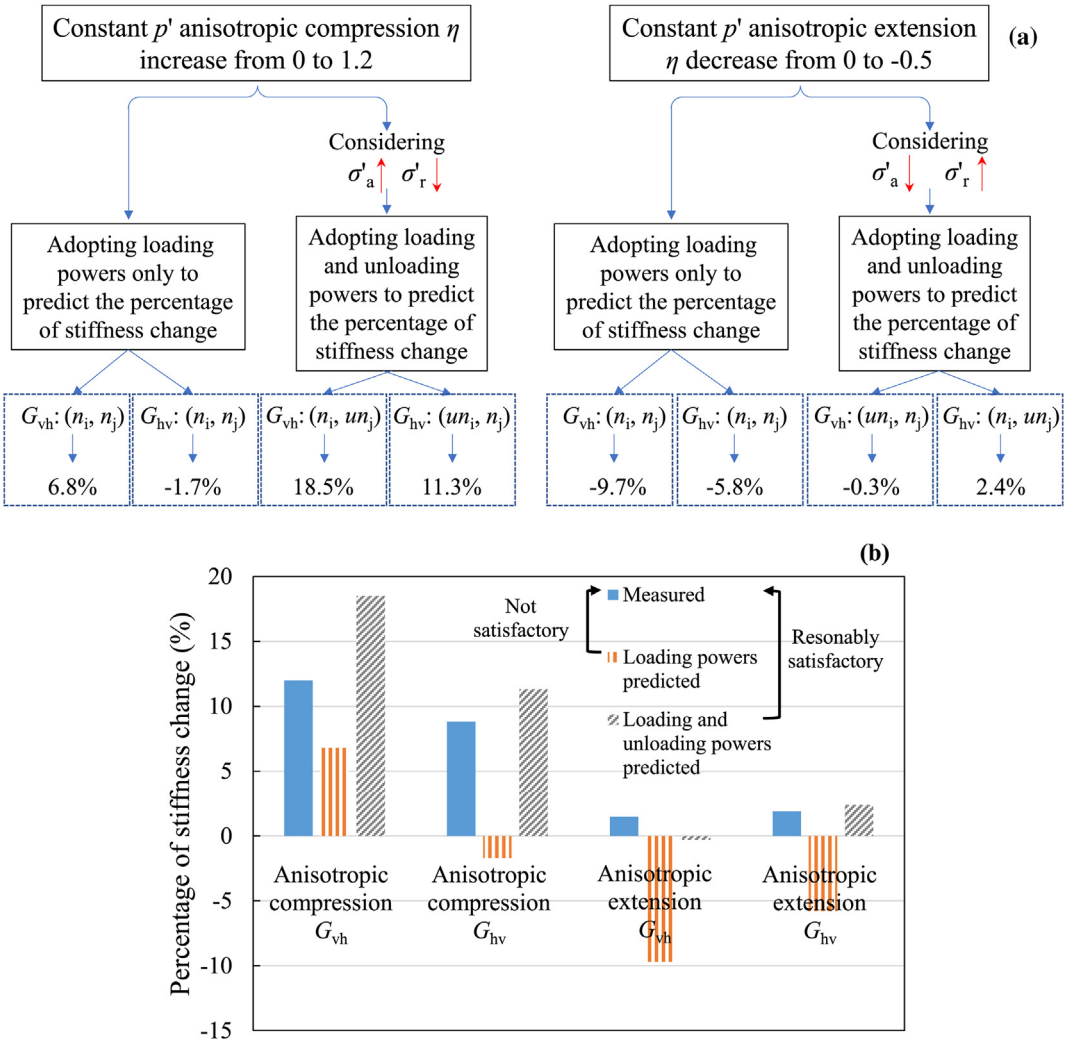

Fig. 15. (a) Flow chart of prediction of the percentage of stiffness components (G_{vh} and G_{hv}) change under constant p' anisotropic compression and extension stress states with different combinations of exponent values (n_i, n_j, un_i and un_j), and (b) Bar chart of the comparison between the predicted and measured percentage of stiffness components change.

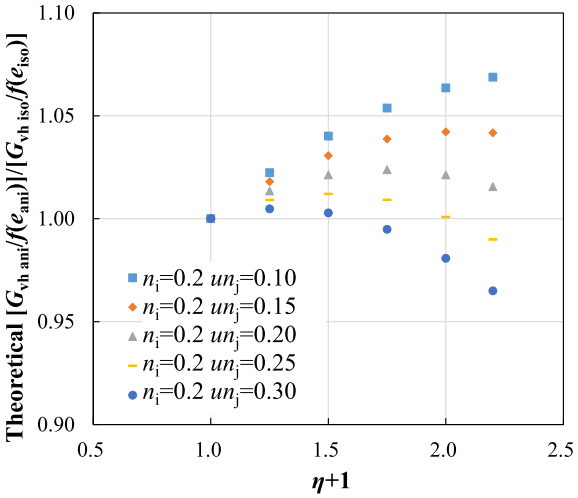

Fig. 16. Theoretical normalised G_{vh}–(η+1) plot with different n_i and n_j combinations.

should be greater than the un_j exponent from the analysis in Fig. 13. This analysis is supported by the experimental work conducted by Payan and Chenari (2019).

4. Conclusions

The stiffness at small strains of two CS, i.e. the WA-CS and the PH-CS, subjected to different types of stress paths was examined. The results stemming from bender element tests on the two CSs were compared with additional tests on three silica sands from different geological origins and different particle shapes, and these silica sands were used as benchmark materials in the study. The conclusions can be drawn as follows:

(1) Under constant p' compression stress paths, the stiffness component G_{vh} of the PH-CS appeared to increase more pronouncedly compared with the WA-CS because of the higher particle angularity of the PH-CS. G_{vh} of both sands was slightly affected by constant p' anisotropic extension stress states. The anisotropic stress history influenced notably the stiffness of both CSs.

(2) Stiffness anisotropy was observed under constant p' stress anisotropy for the PH-CS through the measurements of the stiffness ratio G_{hh}/G_{hv}, and after the removal of the anisotropic stress, the stiffness anisotropy was partly remained due to strain-induced fabric anisotropy. For the LBS, which is a kind of silica sand with rounded grains, the stiffness anisotropy was also evident under anisotropic stress states, but the stiffness anisotropy was negligible after the stress anisotropy was removed.

(3) Through constant axial stress (σ'_a) or radial stress (σ'_r) stress path tests (also referred to as biaxial stress path tests), the exponent n_i, which expresses the sensitivity of stiffness to the stress component in the direction of wave propagation, and n_j, which expresses the sensitivity of stiffness to the stress component in the direction of particle motion, were measured.

(4) It was observed that although the values of the exponent n_i were higher than those of the exponent n_j for the PH-CS, the SS and CR specimens, the difference in magnitude between the n_i and n_j values of the SS was the smallest among the three soils, due to the rounder grain shape of this sand compared with the PH-CS and CR.

(5) Along the unloading of the biaxial stress paths, the CS exhibited much lower unloading exponent values (un_i and un_j) compared with the values observed during the loading process (n_i and n_j).

(6) Comparing the anisotropic stress path and the isotropic stress path test results, the summations of n_i and n_j of the PH-CS and CR, which both have angular particles, were found to be greater than the corresponding n_G values derived from isotropic stress path tests. Nevertheless, the $n_i + n_j$ values of the SS, which consists of rounded particles, matched with the n_G values as predicted from expressions proposed in the literature.

(7) It was proved necessary to adopt the unloading exponent values (un_i and un_j) derived from the biaxial tests, where the stress component decreases, to predict the stiffness satisfactorily along the constant p' compression or extension stress paths. Based on the analysis of the present study together with the existing data published in the literature, it is suggested that for silica sands with angular particles or high coefficients of uniformity, the exponent n_i of the soil should be higher in magnitude compared with its un_j values, which, in turn, indicates that the stiffness is sensitive to constant p' anisotropic loading.

Declaration of competing interest

The authors declare that they have no known competing financial interests or personal relationships that could have appeared to influence the work reported in this paper.

Acknowledgments

The work described in this paper was fully supported by grants from the Research Grants Council of the Hong Kong Special Administrative Region, China (Grant No. CityU 11210419), the Natural Science Foundation of Jiangsu Province (Grant No. BK20200405), and the National Natural Science Foundation of China (Grant No. 52008098).

Appendix A. Supplementary data

Supplementary data to this article can be found online at https://doi.org/10.1016/j.jrmge.2021.03.015.

References

Airey, D., 1993. Triaxial testing of naturally cemented carbonate soil. J. Geotech. Eng. 119 (9), 1379–1398.
Alba, J.L., Audibert, J.M.E., 1999. Pile design in calcareous and carbonaceous granular materials, and historic review. In: Proceedings of the 2nd International Conference on Engineering for Calcareous Sediments. A.A. Balkema, Rotterdam, the Netherlands, pp. 29–44.
Ackerley, S.K., Standing, J.R., Kamal, R.H., 2016. A system for measuring local radial strains in triaxial apparatus. Geotechnique 66 (6), 515–522.
ASTM D2487-11, 2011. Standard Practice for Classification of Soils for Engineering Purposes (Unified Soil Classification System). ASTM International, West Conshohocken, PA, USA.
Bellotti, R., Jamiolkowski, M., Lo Presti, D.C.F., O'Neill, D.A., 1996. Anisotropy of small strain stiffness in Ticino sand. Geotechnique 46 (1), 115–131.
Brandes, H.G., 2011. Geotechnical characteristics of deep-sea sediments from the north atlantic and north pacific oceans. Ocean. Eng. 38 (7), 835–848.
Cho, G.C., Dodds, J., Santamarina, J.C., 2006. Particle shape effects on packing density, stiffness, and strength: natural and crushed sands. J. Geotech. Geoenviron. Eng. 132 (5), 591–602.
Cheng, Z., 2018. Investigation of the Grain-Scale Mechanical Behavior of Granular Soils under Shear Using X-Ray Micro-tomography. PhD Thesis. City University of Hong Kong, Hong Kong, China.
Clayton, C.R.I., 2011. Stiffness at small strain: research and practice. Geotechnique 61 (1), 5–37.
Coop, M.R., 1990. The mechanics of uncemented carbonate sands. Geotechnique 40 (4), 607–626.

Coop, M.R., Atkinson, J.H., 1993. The mechanics of cemented carbonate sands. Geotechnique 43 (1), 53–67.
Coop, M.R., Sorensen, K.K., Freitas, T.B., Georgoutsos, G., 2004. Particle breakage during shearing of a carbonate sand. Geotechnique 54 (3), 157–164.
Fioravante, V., 2000. Anisotropy of small strain stiffness of Ticino and Kenya sands from seismic wave propagation measured in triaxial testing. Soils Found. 40 (4), 129–142.
Fioravante, V., Giretti, D., Jamiolkowski, M., 2013. Small strain stiffness of carbonate Kenya sand. Eng. Geol. 161, 65–80.
Fookes, P.G., 1988. The geology of carbonate soils and rocks and their engineering characterisation and description. In: Proceedings of International Conference of Calcareous Sediments, Perth, pp. 787–806.
Gu, X.Q., Yang, J., Huang, M.S., 2013. DEM simulations of the small strain stiffness of granular soils: effect of stress ratio. Granul. Matter 15 (3), 289–298.
Gu, X.Q., Hu, J., Huang, M.S., 2017. Anisotropy of elasticity and fabric of granular soils. Granul. Matter 19 (2), 33.
Hardin, B.O., Blandford, G.E., 1989. Elasticity of particulate materials. J. Geotech. Eng. 115 (6), 788–805.
He, H., Senetakis, K., 2016. A study of wave velocities and Poisson ratio of recycled concrete aggregate. Soils Found. 56 (4), 593–607.
He, H., Senetakis, K., Ranjith, P.G., 2017a. The behavior of a carbonate sand subjected to a wide strain range of medium-frequency flexural excitation. Geomech. Geophys. Geo-Energy Geo-Resour. 3 (1), 51–60.
He, H., Li, M.N., Senetakis, K., 2017b. A note on the influence of stress anisotropy on Poisson ratio of dry sand. J. Rock Mech. Geotech. Eng. 9 (6), 1159–1164.
He, H., Li, W., Senetakis, K., 2019. Small-strain dynamic behavior of two types of carbonate sands. Soils Found. 59 (3), 571–585.
Ishihara, K., 1996. Soil Behaviour in Earthquake Geotechnics. Oxford University Press, Oxford, UK.
Jafarian, Y., Javdanian, H., 2020. Small-strain dynamic properties of siliceous-carbonate sand under stress anisotropy. Soil Dyn 131, 106045.
Jovicic, V., Coop, M.R., 1997. Stiffness of coarse-grained soils at small strains. Geotechnique 47 (3), 545–561.
King, R., Lodge, M., 1988. North West shelf development—the foundation engineering challenge. In: PRoceedings of the International Conference of Calcareous Sediments, Perth, pp. 333–342.
Knox, D.P., Stokoe, K.H., Kopperman, S.E., 1982. Effect of State of Stress on Velocity of Low-Amplitude Shear Waves Propagating along Principal Stress Directions in Dry Sand. PhD Thesis. University of Texas at Austin, Austin, TX, USA.
Kramer, S.L., 1996. Geotechnical Earthquake Engineering. Prentice-Hall, New Jersey, USA.
Krumbein, W.C., Sloss, L.L., 1963. In: Stratigraphy and Sedimentation, second ed. W.H. Freeman and Company.
Li, W., Senetakis, K., 2017. Dynamic shear modulus of three reconstituted soils from Panzhihua iron tailing dam. J. Geoeng. 12 (3), 129–135.
Liu, X., Li, S., Sun, L.Q., 2020. The study of dynamic properties of carbonate sand through a laboratory database. Bull. Eng. Geol. Environ. 79, 3843–3855.
Lv, Y.R., Liu, J.G., Xiong, Z.M., 2019. One-dimensional dynamic compressive behavior of dry calcareous sand at high strain rates. J. Rock Mech. Geotech. Eng. 11 (1), 192–201.
McClelland, B., 1988. Calcareous sediments: an engineering enigma. In: Proceedings of the 1st International Conference on Calcareous Sediments, Perth, Australia, pp. 777–784.
Miao, G., Airey, D., 2013. Breakage and ultimate states for a carbonate sand. Geotechnique 63 (14), 1221–1229.
Morsy, A.M., Salem, M.A., Elmamlouk, H.H., 2019. Evaluation of dynamic properties of calcareous sands in Egypt at small and medium shear strain ranges. Soil Dyn 116, 692–708.
Nanda, S., Sivakumar, V., Donohue, S., Graham, S., 2018. Small-strain behaviour and crushability of Ballyconnelly carbonate sand under monotonic and cyclic loading. Can. Geotech. J. 55 (7), 979–987.
Ni, S.H., 1987. Dynamic Properties of Sand under True Triaxial Stress States from Resonant Column/torsion Shear Tests. PhD Thesis. University of Texas at Austin, Austin, TX, USA.
Oda, M., Nemat-Nasser, S., Konishi, J., 1985. Stress-induced anisotropy in granular masses. Soils Found. 25 (3), 85–97.
Payan, M., Khoshghalb, A., Senetakis, K., Khalili, N., 2016a. Small-strain stiffness of sand subjected to stress anisotropy. Soil Dyn 88, 143–151.
Payan, M., Khoshghalb, A., Senetakis, K., Khalili, N., 2016b. Effect of particle shape and validity of Gmax models for sand: a critical review and a new expression. Comput. Geotech. 72, 28–41.
Payan, M., Chenari, R.J., 2019. Small strain shear modulus of anisotropically loaded sands. Soil Dyn 125, 105726.
Pennington, D., Nash, D., Lings, M., 2001. Horizontally mounted bender elements for measuring anisotropic shear moduli in triaxial clay specimens. Geotech. Test J. 24 (2), 133–144.
Randolph, M., Gourvenec, S., 2011. Offshore Geotechnical Engineering. CRC Press.
Roesler, S.K., 1979. Anisotropic shear modulus due to stress anisotropy. J. Geotech. Eng. 105 (7), 871–880.
Rothenburg, L., Bathurst, R.J., 1992. Micromechanical features of granular assemblies with planar elliptical particles. Geotechnique 42 (1), 79–95.
Santamarina, J.C., Cascante, G., 1996. Stress anisotropy and wave propagation: a micromechanical view. Can. Geotech. J. 33 (5), 770–782.
Senetakis, K., He, H., 2017. Dynamic characterization of a biogenic sand with a resonant column of fixed-partly fixed boundary conditions. Soil Dyn 95, 180–187.
Shahnazari, H., Rezvani, R., 2013. Effective parameters for the particle breakage of calcareous sands: an experimental study. Eng. Geol. 159, 98–105.
Stokoe, K., Lee, S., Knox, D., 1985. Shear moduli measurements under true triaxial stresses. In: Proceedings of Advances in the Art of Testing Soils under Cyclic Loading Conditions. ASCE, Detroit, pp. 134–142.
Todisco, M.C., Coop, M.R., Pereira, J.M., 2018. Fabric characterisation in transitional soils. Granul. Matter 20 (2), 20.
Viggiani, G., Atkinson, J.H., 1995. Stiffness of fine-grained soil at very small strains. Geotechnique 45 (2), 249–265.
Wang, Y., Ng, C.W.W., 2011. Effects of stress paths on the small-strain stiffness of completely decomposed granite. Can. Geotech. J. 42 (4), 1200–1211.
Wang, X.Z., Jiao, Y.Y., Wang, R., Hu, M.J., Meng, Q.S., Tan, F.Y., 2011. Engineering characteristics of the calcareous sand in Nansha islands, south China sea. Eng. Geol. 120 (1), 40–47.
Wang, X.Z., Wang, X., Jin, Z.C., Meng, Q.S., Zhu, C.Q., Wang, R., 2017. Shear characteristics of calcareous gravelly soil. Bull. Eng. Geol. Environ. 76 (2), 561–573.
Wang, G., Ye, Q.G., Zha, J.J., 2018. Experimental study on mechanical behavior and particle crushing of coral sand-gravel fill. Chin. J. Geotech. Eng. 40 (5), 802–810.
Wang, G., Wang, Z.N., Ye, Q.G., Zha, J.J., 2020. Particle breakage evolution of coral sand using triaxial compression tests. J. Rock Mech. Geotech. Eng. 13 (2), 321–334.
Wees, J.A., Chamberlin, R.S., 1971. Khazzan Dubai no. 1: pile design and installation. J. Soil Mech. Found. Div., Am. Soc. Civ. Eng. 97 (10), 1415–1429.
Wei, H.Z., Zhao, T., He, J.Q., Meng, Q.S., Wang, X.Z., 2018. Evolution of particle breakage for calcareous sands during ring shear tests. Int. J. GeoMech. 18 (2), 04017153.
Yu, P.J., Richart, F.E., 1984. Stress ratio effects on shear modulus of dry sands. J. Geotech. Eng. 110 (3), 331–345.
Yu, F.W., 2018. Particle breakage in triaxial shear of a coral sand. Soils Found. 58 (4), 866–880.

Associate Prof. Huan He received his PhD at the University of New South Wales (Australia) in 2018 and worked as a postdoctoral researcher at City University of Hong Kong before joining Southeast University (China) in 2020. He has been committed to experimental and theoretical research on the dynamics and micromechanics of geomaterials. His research is focused on the dynamic characteristics of natural/artificial crushable granular materials, such as calcareous sands, extrusive igneous rocks and recycled concrete aggregates, through bender/extender element and resonant column testing techniques and tribological-based analyses. In order to bridge the gap between macro- and micro-scale soil mechanics, he designed and built a dynamic micromechanical testing apparatus, with which, new insights into the fundamental behaviour of granular materials and rocks as well as composite interfaces have been revealed. He has published around 20 technical papers in international journals and has received the outstanding reviewer award from the journal *Soils and Foundations*.